# RESEARCH ARTICLE

**Key Points:**
- Contrasting behavior of the $F_2$ peak and the topside ionosphere was observed in response to the 2 October 2013 geomagnetic storm
- Multiple ionospheric observations and model results are used to study ionospheric storm effect during the recovery phase
- The observed contrasting behavior of the $F_2$ peak and the topside ionosphere is primarily associated with neutral winds

**Correspondence to:**
J. Lei,
leijh@ustc.edu.cn

# Contrasting behavior of the $F_2$ peak and the topside ionosphere in response to the 2 October 2013 geomagnetic storm

Jiuhou Lei[1,2,3], Jiahao Zhong[1], Tian Mao[4], Lianhuan Hu[5], Tao Yu[6], Xiaoli Luan[1], Xiankang Dou[1], Eric Sutton[7], Xinan Yue[5], Jian Lin[8], and Inez S. Batista[9]

[1]CAS Key Laboratory of Geospace Environment, School of Earth and Space Sciences, University of Science and Technology of China, Hefei, China, [2]Mengcheng National Geophysical Observatory, University of Science and Technology of China, Hefei, China, [3]Collaborative Innovation Center of Astronautical Science and Technology, Harbin, China, [4]National Satellite Meteorological Center, China Meteorological Administration, Beijing, China, [5]Key Laboratory of Earth and Planetary Physics, Institute of Geology and Geophysics, Chinese Academy of Sciences, Beijing, China, [6]Hubei Subsurface Multi-scale Imaging Key Laboratory, Institute of Geophysics and Geomatics, China University of Geosciences, Wuhan, China, [7]Air Force Research Laboratory, Kirtland, AFB, New Mexico, USA, [8]Institute of Seismology, China Earthquake Administration, Wuhan, China, [9]Instituto Nacional de Pesquisas Espaciais, Sao Jose dos Campos, Brazil

**Abstract** In this study, the ionospheric observations from ionosondes, ground-based GPS receivers, Gravity Recovery and Climate Experiment (GRACE) and MetOp-A satellites, and Fabry-Perot interferometer over the Asian-Australian sector have been used to investigate the responses of the $F_2$ peak and the topside ionosphere to the 2 October 2013 geomagnetic storm, particularly during the recovery phase. The comparison between the multiple simultaneous observations revealed a contrasting behavior of the topside ionosphere and the $F_2$ peak in East Asia during the recovery phase. The upward looking total electron content from low-Earth orbit (LEO) satellites did not undergo such depletions as seen in the region near the $F_2$ peak, and they even showed increases. Furthermore, the simulation results of the Thermosphere Ionosphere Electrodynamics General Circulation Model are used to explore the possible mechanisms responsible for the observed features. The model results and observations suggested that the contrasting behavior of the $F_2$ peak and the topside ionosphere is mainly associated with the enhancement of the equatorward winds, albeit the disturbed electric fields could play an important role in producing it.

## 1. Introduction

The energy and momentum depositions from solar wind and the magnetosphere into the ionosphere and thermosphere (IT) system during storms cause disturbances in dynamical, chemical, and electrodynamical processes of the IT system [e.g., *Burns et al.*, 1995; *Buonsanto*, 1999; *Richmond and Lu*, 2000]. The response of the ionosphere to geomagnetic storms has been widely studied for decades based on the $F_2$ peak density ($N_mF_2$) and total electron content (TEC) [e.g., *Prölss*, 1995; *Mendillo*, 2006, and references therein]. The storm responses of the ionospheric $F$ region are usually considered to be representation of the entire ionospheric behaviors [e.g., *Buonsanto*, 1999; *Mendillo*, 2006], as the ionospheric $F$ region occupies a large proportion of ionospheric plasma. Regarding the topside ionospheric response during storm time, both enhancement and depletion in the topside ionosphere were observed in the topside ionospheric data about 50 years ago [e.g., *Bauer and Krishnamurthy*, 1968; *Arendt*, 1969; *Fatkullin*, 1972]. However, the physical mechanisms for the different topside ionospheric responses were not addressed in these studies. Recently, with more topside ionospheric observations available, studies demonstrated that the topside ionosphere can contribute major increases during storms and/or behave differently from the bottomside ionosphere [e.g., *Belehaki and Tsagouri*, 2002; *Zhao et al.*, 2012; *Lei et al.*, 2014a, 2015; *Zhu et al.*, 2016].

The combination of ionosonde and global positioning system (GPS) TEC or incoherent scatter radar can offer both the topside and bottomside ionospheric behaviors during storms. *Belehaki and Tsagouri* [2002] found that the topside TEC above $F_2$ peak height represented roughly two thirds of the full TEC and that it was strongly affected by geomagnetic activity, much more than the bottomside TEC. *Zhao et al.* [2012] indicated that the electron density in the topside ionosphere had a much stronger enhancement than that in the bottomside ionosphere during a superstorm. However, *Zhu et al.* [2016] found that the relative changes of
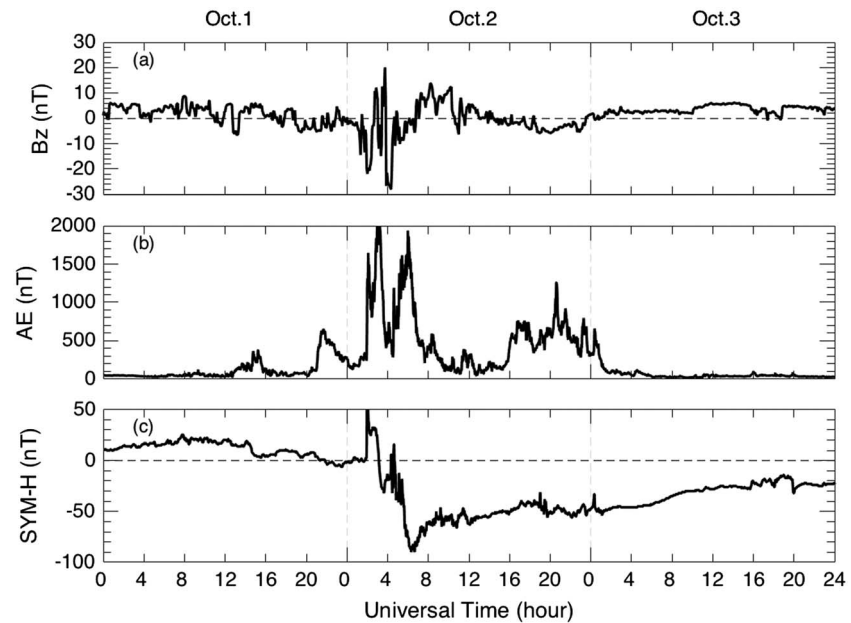
**Figure 1.** Variations of (a) interplanetary magnetic field (IMF) $B_z$ component, (b) the auroral electrojet index *AE*, and (c) *SYM-H* index during 1–3 October 2013.

the topside TEC to the quiet-time reference in two other strong storms were not greater than those of the bottomside TEC and $N_mF_2$. To supplement ground-based observations, low-Earth orbit (LEO) satellite-based TEC measurements can provide a global view of the behavior of topside ionospheric plasma. *Lei et al.* [2015] studied the Halloween superstorms by combining ground-based and LEO-based TECs, and ionosonde data, finding that the increases of LEO-based TEC were more significant than the bottomside ionosphere in response to the ionospheric positive storm, and indicated that TEC changes were not necessarily related to changes in $N_mF_2$.

Previous studies have been devoted to examining the similarities and differences of the $F_2$ peak and the topside ionospheric responses to the main phase of severe storms [e.g., *Lei et al.*, 2015; *Astafyeva et al.*, 2015]. In this paper, the combination of multiple simultaneous ground-based and space-based ionospheric observations over the Asian-Australian sector is utilized to study the responses of the bottomside and topside ionosphere to the 2 October 2013 moderate storm during the recovery phase. Moreover, the simulation results from the Thermosphere Ionosphere Electrodynamics general circulation model (TIEGCM) [*Richmond et al.*, 1992] are used to address the possible physical mechanisms leading to the observed ionospheric response.

## 2. Geophysical Conditions of the October 2013 Storm

The 2 October 2013 storm was caused by a coronal mass ejection with a sudden storm commencement (SSC) time of 01:55 UT (http://isgi.unistra.fr/). Figure 1 shows the variations of the north-south component of the interplanetary magnetic field (IMF) $B_z$, the auroral electrojet index *AE*, and the high-resolution storm index *SYM-H* during 1–3 October 2013. After the SSC, $B_z$ had sharp fluctuations from 02 to 05 UT on 2 October, with two negative excursions of −20 and −25 nT at 02 and 04 UT, respectively. Then $B_z$ turned northward at 07 UT and remained northward until 10 UT. After 12 UT, $B_z$ returned to a normal level. *AE* increased rapidly after the SSC, hovering around 1500 nT from 02 to 06 UT, except for a relatively low value of about 500 nT at 04 UT. *AE* showed a decrease from 07 to 15 UT, but it did not reach a normal level. Later, *AE* increased again at 16 UT and stayed around 600 nT until 24 UT on 2 October. *SYM-H* dropped to a minimum value of about −90 nT at 06:19 UT on 2 October, and then it recovered gradually. According to the work of *Gonzalez et al.* [1994], these features describe a moderate geomagenetic storm. *Mao et al.* [2015] examined the ionospheric response to this storm event over China with ground-based observations, whereas in this study we focused on the ionospheric response during 12–18 UT on 2 October, i.e., during the recovery phase of the storm, by using ground-based and space-based observations, and the TIEGCM simulation.

**Table 1.** Geographic and Geomagnetic Coordinates for the Ground Stations That Provided Ionosonde, GPS TEC, or Neutral Wind Measurements in This Study

| Site | Geographic Latitude | Geographic Longitude | Geomagnetic Latitude | Geomagnetic Longitude |
|------|--------------------|--------------------|--------------------|--------------------|
| Mohe | 52°N | 122.5°E | 46.5°N | 164.0°W |
| Beijing | 40.3°N | 116.2°E | 34.7°N | 170.4°W |
| Kelan | 38.7°N | 111.6°E | 33.2°N | 175.1°W |
| Wuhan | 31°N | 114.5°E | 25.0°N | 172.6°W |
| Nanning | 22.7°N | 109.3°E | 16.3°N | 178.2°W |
| Sanya | 18.3°N | 109.6°E | 11.6°N | 178.1°W |
| Guam | 13.5°N | 144.8°E | 6.0°N | 143.5°W |
| Darwin | 12.4°S | 130.9°E | 21.4°S | 156.3°W |
| Perth | 31.9°S | 115.9°E | 43.6°S | 172.5°W |
| Sao Luis | 2.5°S | 44.2°W | 2.8°S | 27.6°E |

## 3. Data Set and Model Description

In this study, the observations from ionosondes, ground-based GPS receivers, LEO satellites, and Fabry-Perot interferometer (FPI) are used to study the responses of the $F_2$ peak and the topside ionosphere to the 2 October 2013 storm. The geographic and geomagnetic coordinates of the ground stations used in this study are given in Table 1. The orbital information for Gravity Recovery and Climate Experiment (GRACE) and MetOp-A satellites during this storm is shown in Table 2. A brief description of these data sets is given as follows.

1. The ionosondes data obtain from Chinese Meridian project, Global Ionospheric Radio Observatory of the University of Mass Lowell [*Reinisch and Galkin*, 2011], and Bureau of Meteorology, Australia, are used to analyze the behaviors of the $F_2$ peak density ($N_mF_2$) and peak height ($h_mF_2$). The electron density profiles obtained from the manually scaled ionograms at Sanya are used to provide the integrated electron density below the $h_mF_2$ (bottomside TEC). The difference between GPS TEC and ionosonde bottomside TEC is used to study the integrated electron density above $h_mF_2$, which is designated as topside TEC [*Lei et al.*, 2014a, 2015].

2. Ground-based TEC is commonly used to describe the variations of the ionosphere. The relative slant TEC between the ground-based dual-frequency GPS receivers and GPS satellites can be derived using the standard techniques of detection and correction of cycle slips [*Blewitt*, 1990], leveling the carrier-phase observations to the pseudorange observations [*Mannucci et al.*, 1998]. After the GPS satellite biases from International Global Navigation Satellite Systems (GNSS) Service (IGS) and the estimated receiver bias are removed, a geometric mapping function is used to convert the absolute slant GPS TEC to vertical TEC by assuming a spherical shell ionosphere located at 400 km [*Klobuchar*, 1996]. Then the averaged GPS TEC within 40 min sliding window is further used in this study.

3. The TEC measurements above the orbital altitude (upward looking TEC) of GRACE and MetOp-A satellites are derived from their onboard dual-frequency GPS observations. Generally, similar to the processing of ground-based GPS data, before processing the data, the outliers are eliminated, and cycle slips are detected and corrected. The pseudorange TEC is utilized to adjust the level of the carrier-phase TEC in each phase-connected arc. Then the absolute slant TEC can be retrieved after removing the interfrequency biases. The GPS satellite biases are provided by IGS, and the LEO satellite bias is estimated from the least squares algorithm [e.g., *Yue et al.*, 2011; *Zhong et al.*, 2016a, 2016b]. The slant TEC is converted to vertical TEC using a geometry mapping function, and the ionospheric effective height is selected as a function of orbital altitude of the LEO satellite and solar activity [see *Zhong et al.*, 2016c]. To mitigate the error caused by the slant to vertical TEC conversion, the cutoff elevation angle is set as 40° in this

**Table 2.** Orbit Information for the LEO Satellites That Provided Measurements in This Study

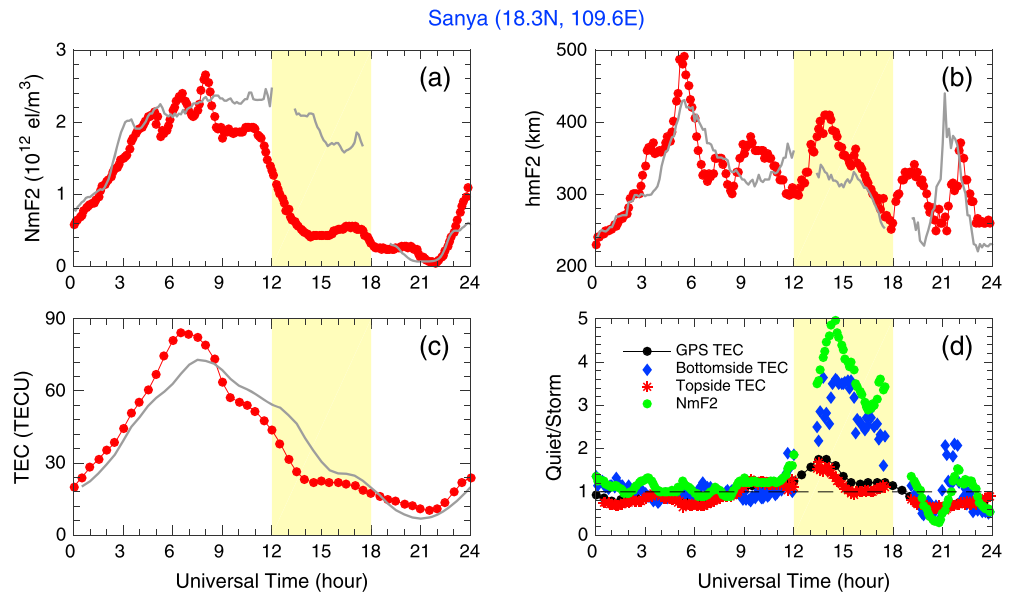| Mission | Altitude | Inclination | Local Time | Type of Observations |
|---------|----------|-------------|------------|---------------------|
| | | | | Upward looking TEC |
| GRACE | 445 km | 89° | 21:24/09:24 | In situ electron density |
| MetOp-A | 832 km | 98.7° | 21:31/09:31 | Upward looking TEC |

Sanya (18.3N, 109.6E)



**Figure 2.** Variations of (a) $N_mF_2$, (b) $h_mF_2$, and (c) GPS TEC observed at Sanya (18.3°N, 109.6°E) on 1 (grey line) and 2 (red line) October 2013. (d) Ratios of the quiet-time TECs and $N_mF_2$ on 1 October to the storm time values on 2 October. The bottomside TEC stands for the integrated electron density below the $F_2$ peak height, and the topside TEC stands for the TEC above the $F_2$ peak height (i.e., the difference between GPS TEC and bottomside TEC). The intervals on which we focused are marked by the yellow bars (LT = UT + 7.3).

study. Overall, the accuracy of the vertical upward looking TEC measurements is adequate for the storm study [e.g., *Zhong et al.*, 2016d] when the relative changes of the topside TECs are focused on.

4. In situ electron densities measured by GRACE are used to supplement the upward looking TEC data. The GRACE mission comprises two identical spacecraft and uses dual-frequency K-band ranging system to measure the intersatellite distance [*Tapley et al.*, 2004]. The TEC between the twin satellites can be calculated from the phase difference in dual K band data. Then the in situ electron densities can be obtained from the TEC by dividing the intersatellite distance. See *Lei et al.* [2014a] for detail. The obtained error of electron densities is suggested to be less than 2–3% [*Lee et al.*, 2011].

5. Neutral wind observations obtained from the Fabry-Perot interferometer over Kelan (38.7°N, 111.6°E) are used to provide dynamical information of the thermosphere. Meridional winds at ~250 km are derived through 630.0 nm nightglow with random errors of about 8–10 m/s [*Yu et al.*, 2014].

The simulation results from the TIEGCM are also used to discuss the physical mechanisms and their contribution to the formation of the observed ionospheric features. The TIEGCM is a first-principle, three-dimensional thermosphere and ionosphere model, which solves the momentum, energy, and continuity equations for neutral and ion species and also includes a self-consistent solution of the middle and low-latitude dynamo electric field [*Richmond et al.*, 1992]. The basic setup and inputs of the TIEGCM are the same as those in *Lei et al.* [2014b] and *Chen et al.* [2016]. In this study, the horizontal resolution of the TIEGCM is 2.5° × 2.5°, and the vertical resolution is one fourth scale height. Solar wind and IMF data with 4 min time resolution from ACE satellite are used as the inputs to the TIEGCM to specify the high-latitude convection pattern using the Weimer model [*Weimer*, 2005].

## 4. Ionospheric Observations

Figures 2a and 2c show the diurnal variations of $N_mF_2$, $h_mF_2$ and GPS TEC observed at Sanya (18.3°N, 109.6°E) on 1 and 2 October 2013. As seen in Figure 2a, the $N_mF_2$ on 2 October (red line) during 03–08 UT (the storm main phase) was comparable with that on 1 October (grey line), except that it had many oscillations, which could be associated with large-scale traveling ionospheric disturbances (TIDs). The oscillation features become more evident in the $h_mF_2$ plot in Figure 2b. The GPS TEC increased from ~04 UT and reached ~80 total electron content unit (TECU, 1 TECU = $10^{16}$ el m$^{-2}$) at 07 UT. Compared with the quiet-time reference, the maximum TEC enhancement at Sanya was about 25 TECU at 05 UT on 2 October. *Mao et al.* [2015]
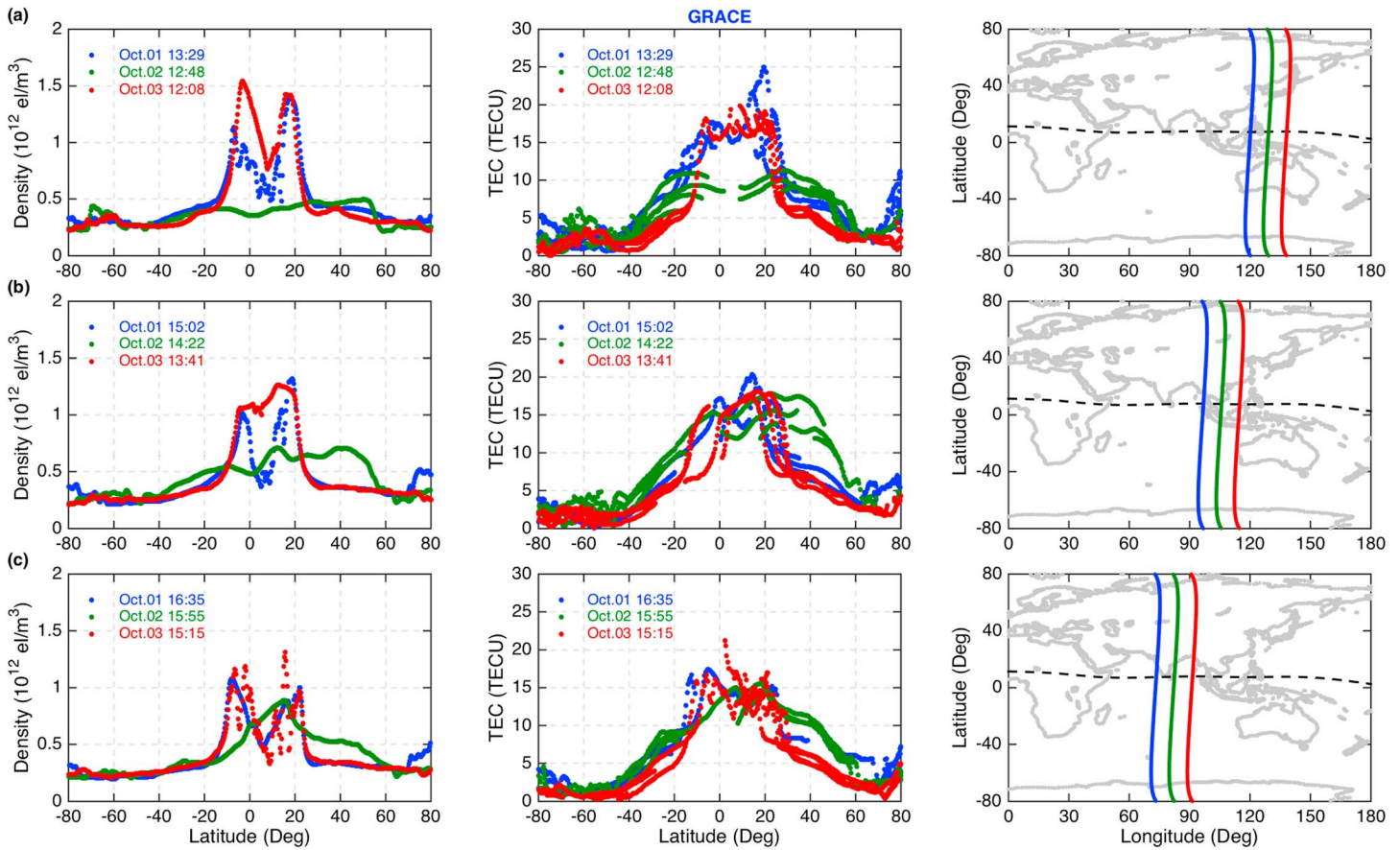
**Figure 3.** (left column) Electron densities and (middle column) upward looking TECs from GRACE satellite during 1–3 October 2013. The blue, red, and green dots represent the values on 1–3 October, respectively. The UTs when the satellite passed over the equator for each orbit are given in the top left corner. The corresponding (right column) orbital paths as a function of geographic latitude and longitude are also shown. The dashed lines represent the magnetic dip equator.

suggested that this positive ionosphere phase seen in the TEC during the main phase is attributed to eastward prompt penetration electric fields (PPEF), and that these TIDs are associated with neutral wind surges or traveling atmospheric disturbances (TADs). It is clear that the $N_mF_2$ and TEC showed different behavior during the main phase. Specifically, the positive ionospheric phase was observed in the TEC data, but both positive and negative ionospheric phases were seen in $N_mF_2$.

After the storm main phase, $N_mF_2$ decreased considerably at 08–09 UT, and it showed a sharp depletion again with an excursion of $1.5 \times 10^{12}$ el/m$^3$ from 11:30 to 14:00 UT. Consequently, the $N_mF_2$ underwent a prominent negative phase during 12–18 UT. As for $h_mF_2$, it oscillated continuously as it did during the main phase. The GPS TEC on 2 October was also lower than the quiet-time values from 08:30 to 18:00 UT, but the relative decrease of GPS TEC was much smaller than that of $N_mF_2$. Figure 2d shows the ratios of the quiet-time TECs and $N_mF_2$ on 1 October with respect to the storm time values on 2 October. The ratio greater than unity represents a decrease or negative storm phase. It is immediately evident that the TECs and $N_mF_2$ during the storm main phase (03–08 UT) were generally similar to those of quiet time. During 12–18 UT, the $N_mF_2$ on 2 October decreased by a factor of 3–5 with respect to the quiet-time reference, and the bottomside TEC showed 2–3.5 times less. However, the GPS TEC and topside TEC were lower by a factor of about 1.2–1.8 than the quiet-time values. Overall, during 12–18 UT on 2 October, the GPS TEC and topside TEC did not have such profound depletions as seen in $N_mF_2$ and bottomside TEC. Next, we focus on the contrasting behavior of the $F_2$ peak and the topside ionosphere during 12–18 UT of the recovery phase.

Figure 3 shows the in situ electron density and upward looking TEC observations from GRACE satellite over the Asian-Australian sector during 1–3 October. The local time sampling of these observations at low and middle latitudes was about 21:24 LT. As shown in Figure 3a (around 12:45 UT), the electron densities on
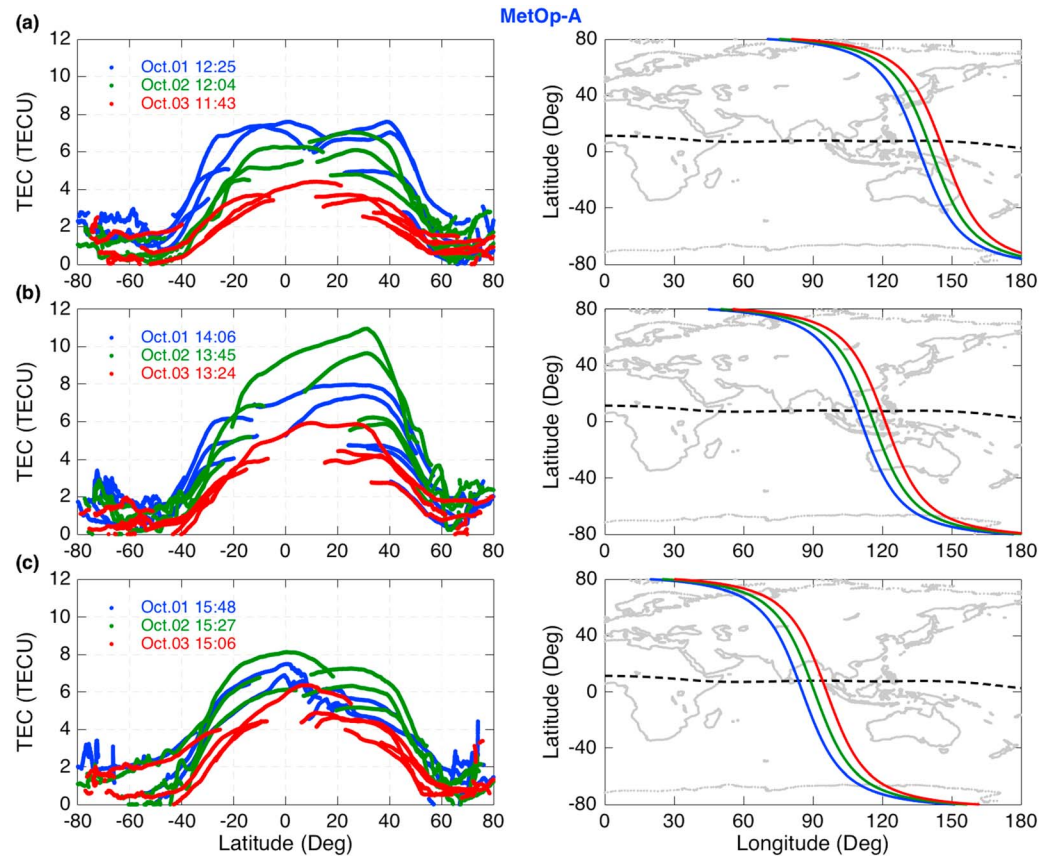
**Figure 4.** (left column) Upward looking TECs from MetOp-A satellite during 1–3 October 2013. The blue, red, and green dots represent the values on 1–3 October, respectively. The UTs when the satellite passed over the equator for each orbit are given in the top left corner. The corresponding (right column) orbital paths as a function of geographic latitude and longitude are also shown. The dashed lines represent the magnetic dip equator.

1 and 3 October (blue and red dots) showed obvious double-crest structure, whereas the electron densities on 2 October (green dots) were about $4 \times 10^{11}$ el/m$^3$ and varied little with latitudes. In addition, a small increase was observed at 50°N latitude on 2 October. The upward looking TEC at low latitudes also showed a decrease of 10 TECU compared with the quiet-time levels. At around 14:20 UT (Figure 3b), when GRACE passed over longitudes around Sanya, the electron densities on 2 October also showed an obvious decrease at low latitudes. Additionally, the electron densities at 30°N–50°N latitudes showed an increase. However, the upward looking TEC was comparable with the quiet-time value at low latitudes. These results indicate that there was a quite different response between the topside ionosphere and the $F_2$ peak at low latitudes. An increase of upward looking TEC at middle latitudes in the Northern Hemisphere was also observed. In Figure 3c (around 15:55 UT), the electron densities on 2 October showed a single crest around 15°N latitude and an increase at middle latitudes in the Northern Hemisphere. The upward looking TEC was generally comparable with the quiet-time level, though it was a little lower at 20°S–0° latitudes and slightly greater at middle latitudes in the Northern Hemisphere. Overall, the topside ionosphere behaved differently from the $F_2$ peak around the longitude of 110°E.

The upward looking TECs of MetOp-A satellite (21:31 LT), which shared a similar orbital local time with GRACE, were also utilized to analyze the behavior of the topside ionosphere around 110°E longitude. In Figure 4a (around 12:00 UT), the upward looking TEC on 2 October was a little smaller than the quiet-time TEC on 1 October. When MetOp-A passed over around Sanya (Figure 4b, 13:45 UT), the upward looking TEC was obviously greater than the quiet-time TEC at low latitudes with a peak value around 30°N latitude. In Figure 4c, the upward looking TEC was a little greater than the quiet-time TEC at low latitudes. These results indicate that, at low latitudes around the 110°E longitude, the upward looking TEC above 832 km was comparable with and even greater than the quiet-time reference.
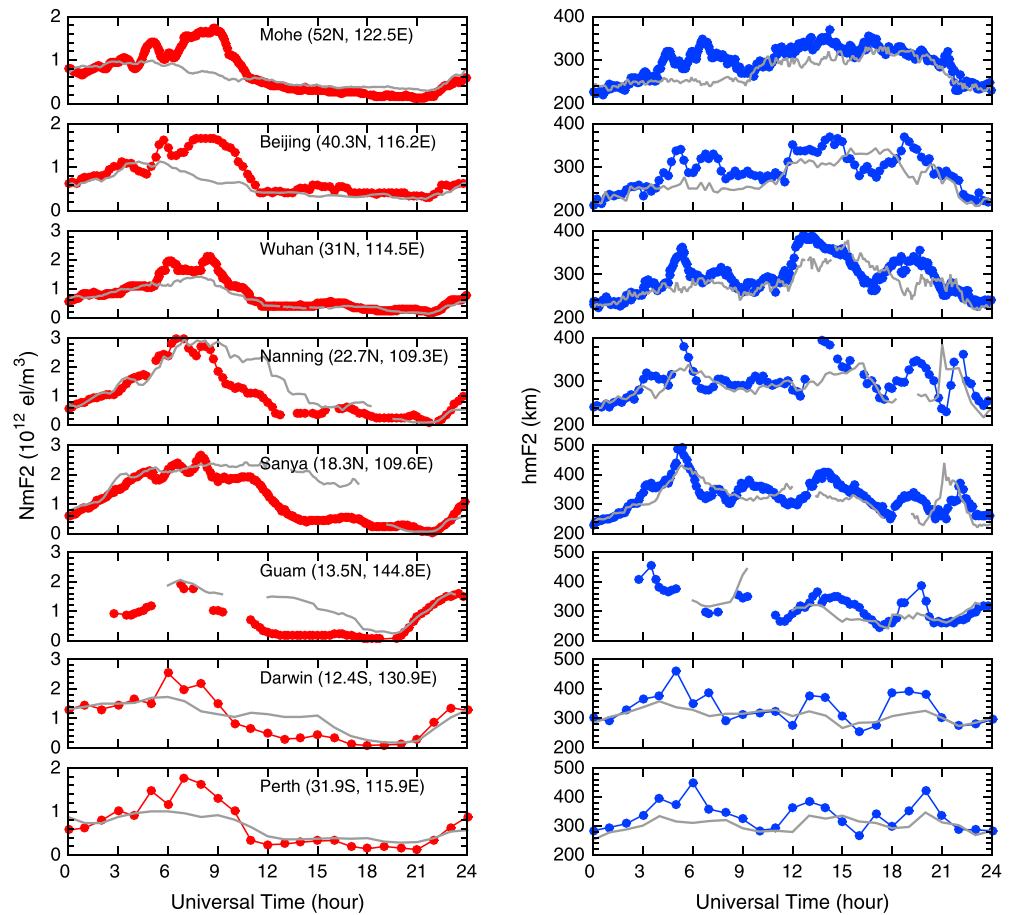
**Figure 5.** Variations of (left column) $N_mF_2$ and (right column) $h_mF_2$ at ionosonde stations over the East Asian and Australian sector on 2 (red or blue lines) and 1 (grey lines) October 2013.

As shown in Figures 3 and 4, the observations from GRACE and MetOp-A satellites showed a consistent pattern, and they indicate that the contrasting behavior of the topside ionosphere and the $F_2$ peak around Sanya during 12–18 UT of the recovery phase is associated with the absent depletion in the topside ionosphere. To give latitudinal variations of this ionospheric feature, Figure 5 shows the $N_mF_2$ and $h_mF_2$ observations at multiple ionosonde stations along the Asian-Australian sector during 1–2 October 2013. At higher latitudes, the $N_mF_2$ at Mohe, Beijing, Wuhan, Darwin, and Perth underwent obvious enhancements during 05–08 UT on 2 October. Again, these enhancements during the main phase could be caused by the daytime eastward PPEF [Mao et al., 2015]. The $N_mF_2$ at Mohe, Beijing, Wuhan, and Perth reduced to their quiet-time values after about 11 UT. However, the $N_mF_2$ at Nanning, Sanya, Guam, and Darwin became lower than their quiet-time levels from about 09 to 18 UT, and the differences were most obvious at 12–15 UT. The $h_mF_2$ at all stations had similar oscillation features as seen in those at Sanya. Therefore, besides electric field, TADs further modulated the storm time ionospheric response.

Given that the $N_mF_2$ at Guam and Darwin during 12–18 UT on 2 October also exhibited prominent depletions as those at Sanya had, the corresponding GPS TEC data are compared with the $N_mF_2$ (Figure 6). As shown in Figures 6a and 6b, the TEC at both Guam and Darwin showed positive ionospheric phase during the main phase and negative ionospheric phase during the recovery phase. However, during the recovery phase, the ratios of the quiet-time TECs with respect to the storm time values on 2 October were only slightly lower than those of the $N_mF_2$ (Figures 6c and 6d). Thus, unlike at Sanya, the responses of the $F_2$ peak and the topside ionosphere to this storm during the recovery phase were similar at Guam and Darwin.
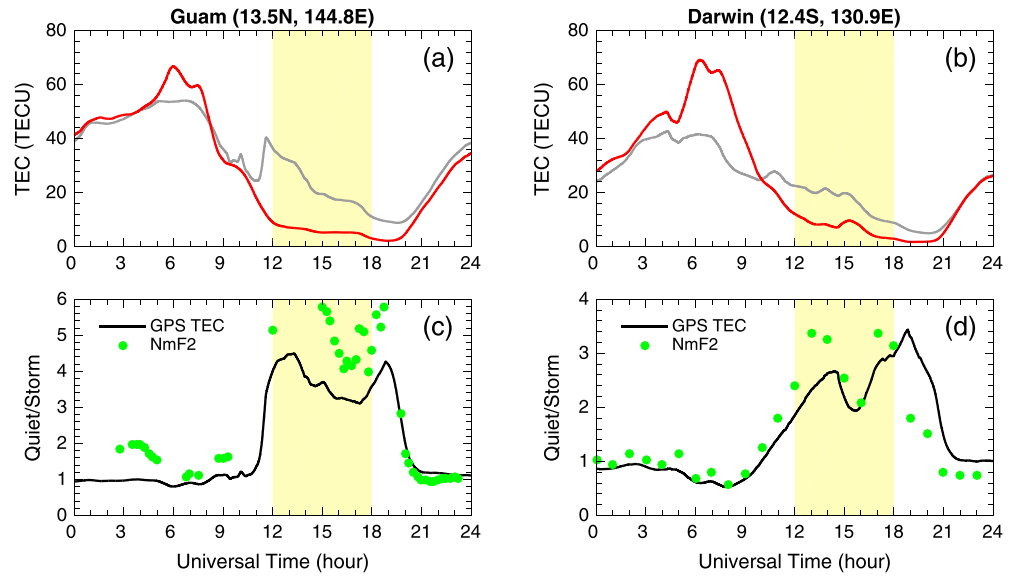
**Figure 6.** (a and b) GPS TEC observed at Guam and Darwin on 1 (grey line) and 2 (red line) October 2013, and (c and d) ratios of the quiet-time TECs and $N_mF_2$ on 1 October with respect to those on 2 October. The intervals on which we focused are marked by the yellow bars.
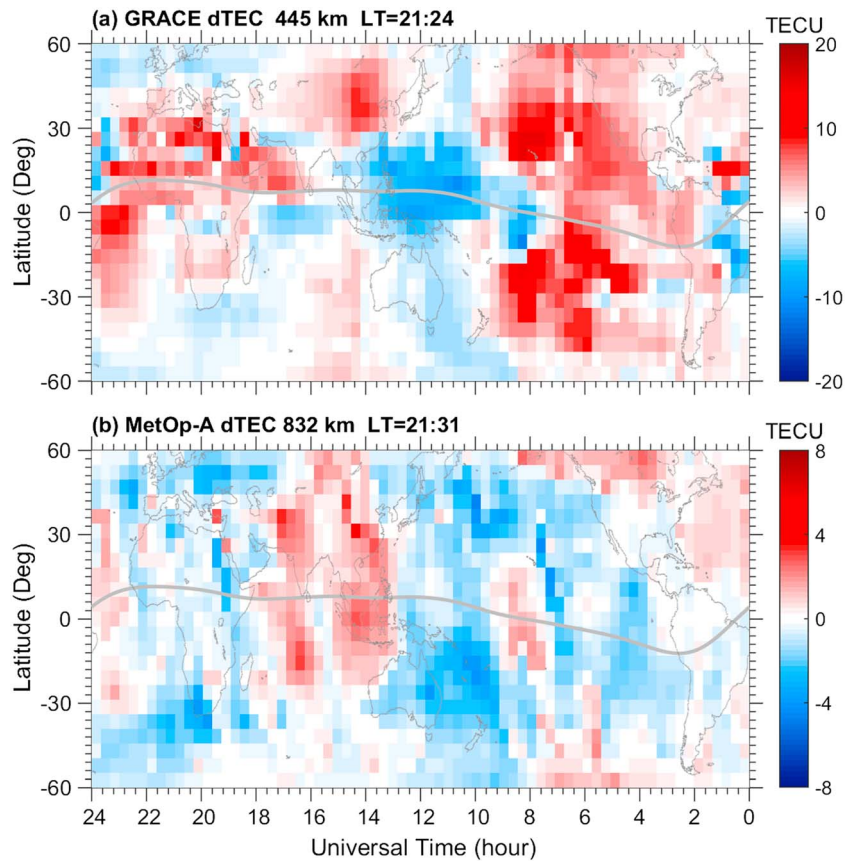


**Figure 7.** Changes of upward looking TEC from (a) GRACE and (b) MetOp-A satellites in the evening sector on 2 October (time goes from right to left). The TEC data on 1 October are used as quiet-time references. The maps are obtained from two-dimensional interpolation of the satellite data for better visualization.

To give the global distribution of the upward looking TEC differences, Figure 7 shows the changes of upward looking vertical TECs from GRACE and MetOp-A satellites in the evening orbits on the whole day, 2 October. As previously mentioned, GRACE and MetOp-A satellites had the similar orbital local time. A contrasting behavior in the pattern of TEC differences is observed between GRACE and MetOp-A TECs above the Pacific Ocean during 03–09 UT. During this period, the increase of the GRACE TEC and the decrease of the MetOp-A TEC suggest that the TEC enhancements occurred mainly below 830 km. The PPEF could also occur in this evening sector in the initial and main phases, a similar condition of the October 2003 storms as reported in *Lei et al.* [2015]. At 09–13 UT, the GRACE TECs showed a strong depletion around the equatorial region, and the MetOp-A TECs also had depletions over the eastern Pacific Ocean and over Australia. During 13–17 UT, the GRACE TEC in the equatorial region (southern Asia) showed a weak decrease, but it underwent an increase at the low and middle latitudes. However, the MetOp-A TEC had enhancements in the southern Asia during 13–17 UT. This is consistent with the results in Figures 2 and 6 that the relative depletion in TEC is much less than that in $N_mF_2$ over Sanya as compared with the results at Guam and Darwin. Thus, the LEO TECs confirmed the contrasting picture of the $F_2$ peak and the topside ionosphere at low latitudes over the Asian-Australian sector during 12–18 UT in response to the 2 October 2013 geomagnetic storm.

In summary, the ionosonde-observed $N_mF_2$ at low latitudes showed a profound decrease during the recovery phase as compared with the quiet-time level, but the topside TEC and LEO-based TEC did not have such depletions and they even showed increases, especially at low latitudes over East Asia. In the next section, we discuss the possible mechanisms responsible for this contrasting behavior of the $F_2$ peak and the topside ionosphere.

## 5. Possible Physical Mechanisms for the Contrasting Feature of the $F_2$ Peak and the Topside Ionosphere

In this study, the combination of multiple simultaneous ionospheric observations provides a contrasting picture of the $F_2$ peak and the topside ionosphere at low latitudes over the Asian-Australian sector during 12–18 UT (recovery phase) in response to the 2 October 2013 geomagnetic storm. It was found that the $N_mF_2$ at Sanya decreased by a factor of 3–5 with respect to the quiet-time level, and the bottomside TEC showed a similar depletion, while the topside ionospheric electron density did not change or even increased. Generally, the responses of ionospheric variations at low and middle latitudes to geomagnetic storms can be associated with neutral winds, electric fields, and neutral composition. During the recovery phase of this storm, the storm time neutral composition disturbances could contribute to topside ionospheric depletions over the southern Pacific Ocean and Australia (Figures 6 and 7), the near-pole region [*Rishbeth*, 1998]. As a result, both the $F_2$ peak density and topside ionospheric electron densities underwent significant decreases. This explains why the $N_mF_2$ and TEC depletions at Guam and Darwin were similar. Nevertheless, in Figures 3, 5, and 7 there were no remarkable decreases observed in the $N_mF_2$ and TEC at high or middle latitudes in the Northern Hemisphere during the recovery phase. Thus, the contrasting behavior of the topside ionosphere and the $F_2$ peak in Southeast Asia is unlikely to be caused by the neutral composition effect extended from high latitudes of the Northern Hemisphere.

In this section, we mainly use TIEGCM results to assess the thermospheric dynamic effect on the ionospheric behavior during the recovery phase. Before going to discuss the possible contributions of neutral winds and electric field, we first concentrate on the simulated $N_mF_2$ and $h_mF_2$. Figure 8 shows the variations of the TIEGCM-simulated $N_mF_2$ and $h_mF_2$ at latitudes of 41.25°N, 18.75°N, 13.75°S, and 31.25°S along the longitude of 110°E on 1 and 2 October 2013. The positive storm effect is seen in $N_mF_2$ at the latitudes of 41.25°N, 13.75°S, and 31.25°S during 04–09 UT of the main phase; subsequently, the negative storm effect persists during the storm recovery phase. However, at the location of 18.75°N, the negative storm effect starts at an earlier time, i.e., 05 UT (Figure 8b). The simulated $h_mF_2$ at all latitudes shows three or even more oscillations on 2 October. Overall, the model reproduced the main features seen in the observed $N_mF_2$ and $h_mF_2$ in Figure 5.

It should be pointed out that, at 18.75°N and 13.75°S (Figures 8b and 8c), the negative storm effects during the recovery phase are much weaker in the simulated $N_mF_2$ as compared with the observations at similar latitudes (cf. Sanya and Guam in Figure 5). This could be associated with the fact that the upper boundary of the TIEGCM locates at about 500–600 km for this case. In addition, the upper boundary for the given $O^+$ flux as a
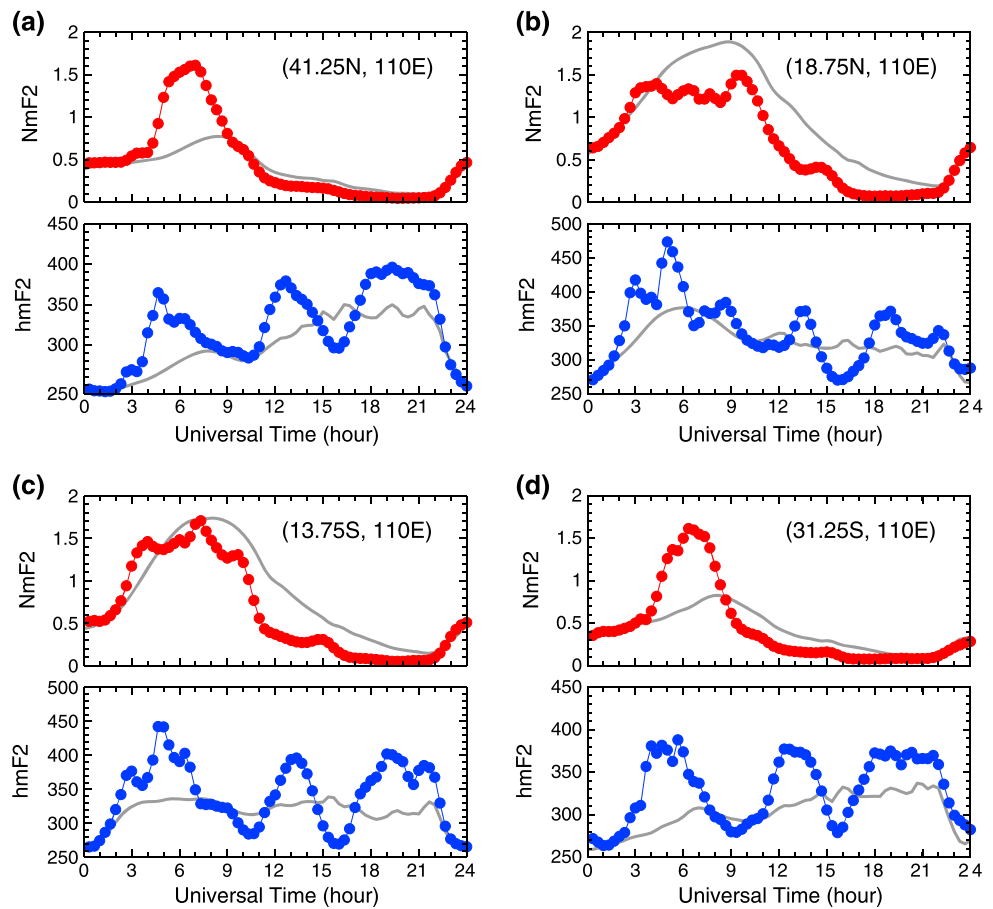
**Figure 8.** Variations of the TIEGCM-simulated $N_mF_2$ (in units of $10^{12}\,m^{-3}$) and $h_mF_2$ (in units of kilometer) on 1 (grey line) and 2 (solid line with dots) October 2013. The simulations at latitudes of (a) 41.25°N, (b) 18.75°N, (c) 13.75°S, and (d) 31.25°S along the longitude 110°E are shown.

function of magnetic latitude does not vary with geophysical conditions. The downward flux in the model might be underestimated significantly, leading to a lower quiet-time $N_mF_2$ level at low latitudes during 09–18 UT. Since the TIEGCM has an upper limit of 500–600 km in altitude, the simulated electron densities are improper to assess the observed contrasting behavior of the topside ionosphere and the $F_2$ peak. Instead, we focus on the simulated neutral winds and electric field to explore the main forming mechanism of the observed disturbances.

Figure 9 gives a comparison of the TIEGCM-simulated $h_mF_2$, meridional winds (equatorward positive) and vertical E × B drift (upward positive) at about 300 km on 1 and 2 October 2013. It is clear that the increases of $h_mF_2$ and $N_mF_2$ at four latitudes during 03–07 UT on 2 October are mainly associated with the enhancement of the vertical drift due to the PPEF, although during the late main phase (i.e., 05–07 UT) the enhanced equatorward winds could play a role in uplifting the ionosphere, except at the latitude of 18.75°N where neutral winds only show slight changes. $N_mF_2$ at 41.25°N and 31.25°S start to fall rapidly at about 07 UT on 2 October. This feature could be related with the return of vertical drift at about 07 UT to the quiet-time level. Without the support of the stronger vertical drift, the changed electron density profiles cannot hold any more, the enhanced ambipolar diffusion could cause the decrease of plasma and even result in a negative ionospheric phase. It is interesting to note that the one-to-one correspondence of the oscillations between neutral winds and $h_mF_2$ is clearly seen in the considered latitudes in Figure 9. However, whether and how the neutral wind surges/oscillations are related with the TADs are beyond the scope of this study.

Figure 10 shows the comparison of meridional winds at about 250 km from the simulation and observed by Fabry-Perot interferometer at Kelan (38.7°N, 111.6°E). This comparison provides a kind of validation of
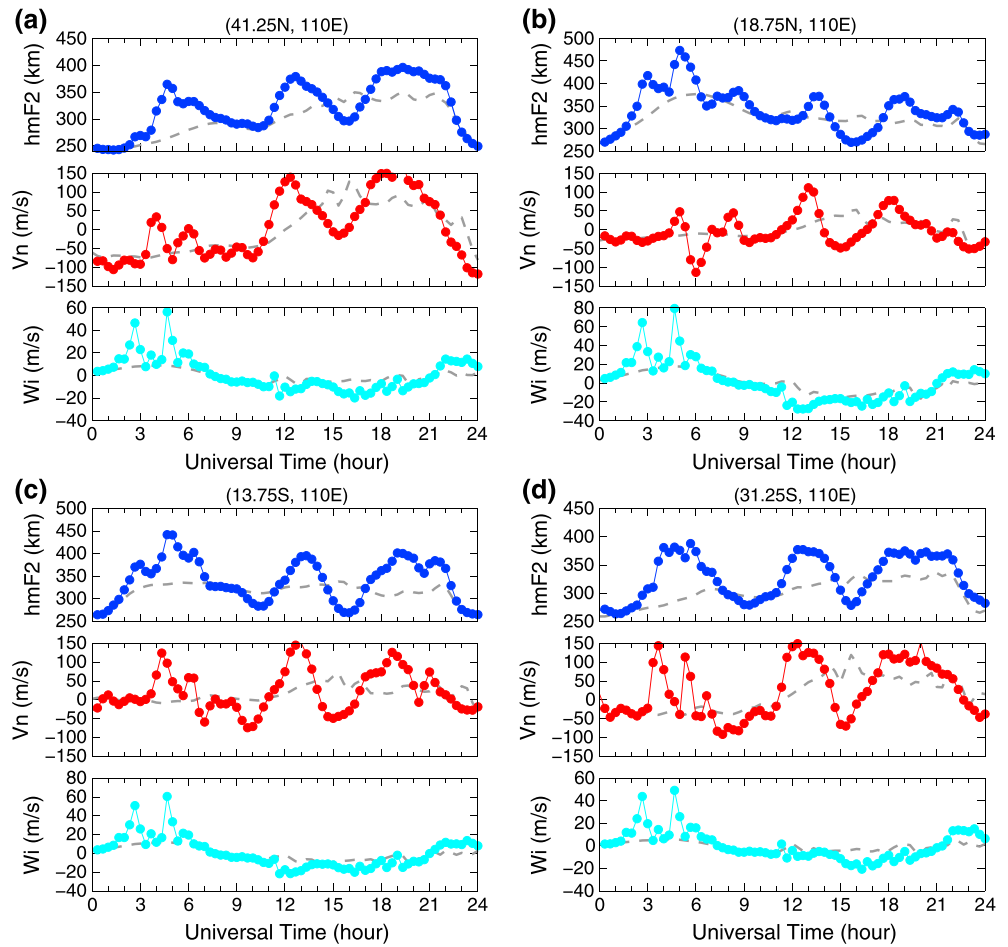
**Figure 9.** Variations of the TIEGCM-simulated $h_mF_2$, meridional winds (equatorward positive) and vertical E×B drift (upward positive) at about 300 km on 1 (grey dashed line) and 2 (solid line with dots) October 2013. The simulations at latitudes of (a) 41.25°N, (b) 18.75°N, (c) 13.75°S, and (d) 31.25°S along the longitude 110°E are shown.
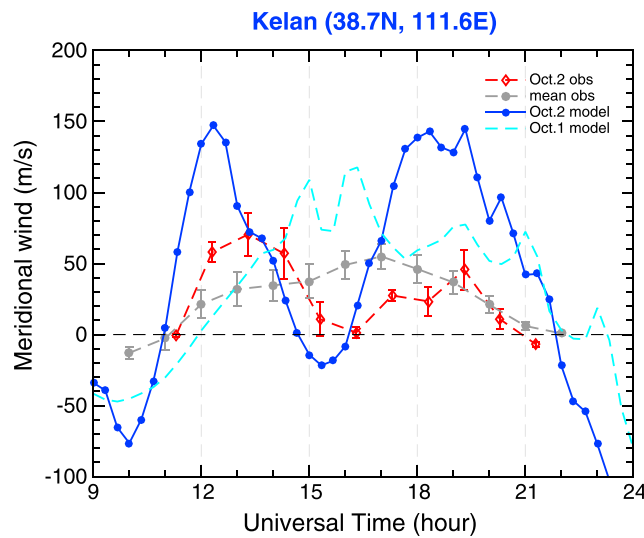


**Figure 10.** Comparison of meridional winds (equatorward positive) at around 250 km observed by FPI at Kelan with the TIEGCM winds on 2 October 2013. The monthly averaged FPI winds with standard deviations (grey) and the TIEGCM winds on 1 October 2013 are also shown as the reference.

the simulated neutral winds. Due to cloudy weather on 1 October, the monthly averaged winds were used for the quiet-time reference. From 12 to 14 UT on 2 October, there was an obvious enhancement in the equatorward wind. Subsequently, the equatorward wind showed a rapid decrease, reduced from 50 m/s at 14 UT to 0 m/s at 16 UT. Later, the equatorward wind returned to the quiet-time level at ~19 UT, but it showed a decrease again afterward. Overall, the equatorward wind presented wind surges during 13–14 UT and 19–20 UT. The TIEGCM reproduced these two wind surges, albeit the simulated equatorward winds on both 1 and 2 October are larger than the observed. The TIEGCM
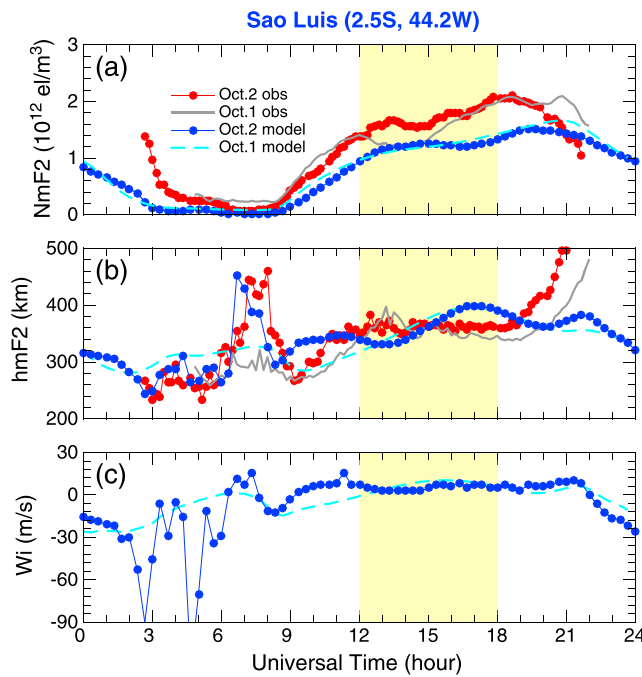
**Figure 11.** Variations of the observed and simulated (a) $N_mF_2$ and (b) $h_mF_2$, and (c) the TIEGCM vertical drifts due to electric field at Sao Luis on 1 and 2 October 2013. The intervals on which we focused are marked by the yellow bars.

simulation and GRACE thermospheric density data (not shown) also indicated that the weaker equatorward winds around 16 UT could be associated with the equatorward propagation of the TAD from the Southern Hemisphere. Note that the Fabry-Perot interferometer observations at Darwin also showed an equatorward wind surge around 13 UT and a stronger poleward winds during 15–17 UT on 2 October (http://stdb2.stelab.nagoya-u.ac.jp/omti/data/data.html). Unfortunately, neutral wind data during 13–15 UT were unavailable at Darwin due to cloudy weather. Again, our simulation clearly demonstrated that the meridional wind variations during the recovery phase are the dominant contributor to the changes of $h_mF_2$, as shown in Figure 9. The equatorward wind would push the plasma upward along the magnetic field line, while the effect of the poleward wind becomes opposite. As the equatorw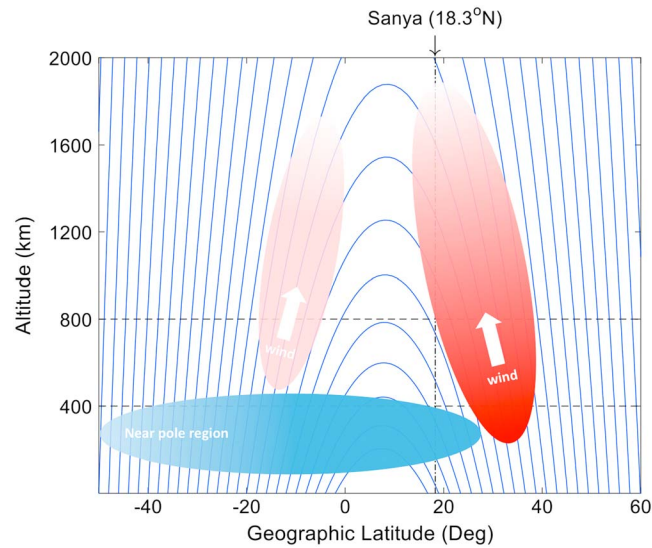ard wind observed at Kelan was greater at 12–15 and 18–21 UT, the $h_mF_2$ at middle-latitude sites (Beijing and Wuhan) was higher at the same time, and the $h_mF_2$ at low-latitude sites also changed correspondingly, but took place at later times (see Figures 5 and 9). As stated above, the oscillations of $h_mF_2$ during the recovery phase can be explained by the wind oscillations, as indicated by the simulation and FPI data (Figures 9 and 10).

It is worth noting that in Figure 5 the $h_mF_2$ increase at Guam during the recovery phase cannot be simply explained by the neutral wind mechanical effect, because in the equatorial region, the geomagnetic field lines are nearly horizontal so that neutral winds are usually inefficient in elevating $h_mF_2$. Another possible contributor for the $h_mF_2$ enhancement in the equatorial region is the ionospheric electric field. It is well known that an eastward electric field can cause $E \times B$ upward drift, which results in elevating $h_mF_2$. As seen in Figure 9, the simulated vertical drift tends to be more downward during the recovery phase as compared with the quiet-time values. Again, the increase of $h_mF_2$ during the recovery phase is attributed to the enhanced equatorward winds rather than electric field from the simulation result perspective. Unfortunately, there is no direct electric field measurement at East Asia to validate the simulated electric field. Figure 11 shows the $N_mF_2$ and $h_mF_2$ observed at Sao Luis in South America to provide indirect information of ionospheric electric field. If the nightside $h_mF_2$ in East Asia was elevating by an eastward electric field, according to the theory of the ionospheric disturbance dynamo [*Blanc and Richmond*, 1980], then a westward electric field should present at dayside, and vice versa. In Figure 11, the $N_mF_2$ at Sao Luis around the magnetic equator showed an increase at 13–14 UT on 2 October with respect to the quiet values, and the corresponding $h_mF_2$ had a slight decline during this period. This implies that a weak westward electric field associated with wind disturbance dynamo could happen in the American sector during the recovery phase.

The simulated $N_mF_2$ and $h_mF_2$ at Sao Luis are also shown in Figure 11 for comparison. The simulated $N_mF_2$ in daytime is lower than the observed $N_mF_2$. For $h_mF_2$, the TIEGCM overestimates the observed values during 15–19 UT. Nevertheless, the TIEGCM generally reproduces the changes of $N_mF_2$ and $h_mF_2$ associated with the storm effect. The TIEGCM predicts the enhancement of the $h_mF_2$ around 06–09 UT on 2 October. Furthermore, the simulation shows an increase of $h_mF_2$, accompanying with a slight decrease of $N_mF_2$ during 08–12 UT, and then a decrease of $h_mF_2$ with a weak increase of $N_mF_2$ during 12–16 UT. This pattern is

**Figure 12.** Sketch illustrating the contrasting response of the topside ionosphere and the $F_2$ peak at longitude 110° to the recovery phase of the October 2013 storm. Red and blue colors represent enhancement and depletion of electron densities, respectively.

consistent with the observations. The simulation also indicates that the weak changes in the daytime $N_mF_2$ and $h_mF_2$ are mainly due to the corresponding changes of vertical drifts (Figure 11c) possibly associated with the disturbance dynamo electric field. Both the simulation and observation imply that a weak westward electric field could happen in the American sector during the recovery phase. Referring back to Figure 9, the TIEGCM results show downward vertical drifts in the Asian nighttime sector during this recovery phase, which could be also modulated by the nighttime PPEFs. Thus, the contribution of the changes in electric field to the formation of the observed contrasting behavior of the $F_2$ peak and the topside ionosphere should be less significant.

*Lei et al.* [2014a, 2015] revealed different responses between the topside and bottomside ionosphere to two superstorms of October 2003. They suggested that the PPEFs during the superstorms contribute the prominent enhancement in the topside TEC. As shown in Figure 5, the $N_mF_2$ at Sanya and Guam did not have notable changes during the main phase of this storm event, but the GPS TEC increased clearly (Figures 2 and 6). This contrasting feature at Sanya and Guam could be associated with the stretch of electron density profiles at low latitudes due to the PPEF. However, as discussed above, during the recovery phase although disturbed electric field also plays a significant role, neutral winds could be the dominant contributor in producing the contrasting behavior of the $F_2$ peak and the topside ionosphere at low latitudes in southern Asia. The following scenario is used to explain this enhancement of the topside plasma. Since the topside ionosphere at low latitudes is connected with the region near the $F_2$ peak at middle latitudes by the flux tube, an enhanced equatorward wind tends to push more plasma at middle latitudes from the region near the $F_2$ peak into the topside ionosphere. Consequently, the upward looking TEC in the equatorial and low-latitude regions can undergo an obvious enhancement. A schematic plot in Figure 12 is used to illustrate this scenario. Here we emphasize the contribution of the $F$ region ionosphere at low and middle latitudes, which provides a source for the enhancement of the topside ionosphere in the equatorial region. Therefore, besides electric field as demonstrated in *Lei et al.* [2014a, 2015], neutral winds can act as an important driver for the storm-related different responses between the bottomside and topside ionosphere. A coupled ionosphere-thermosphere model with a plasmasphere module is desired to test this hypothesis in the future. In addition, the possible association of the observed features during this recovery phase with plasmaspheric refilling [*Singh and Horwitz*, 1992] is also worth further investigation. A final note to be added is that superstorm conditions are not necessary to observe different responses of the bottomside and topside ionosphere during storm time.

## 6. Summary

In this paper, we focused on the contrasting behavior of the $F_2$ peak and the topside ionosphere in response to the 2 October 2013 geomagnetic storm during the recovery phase by combining multiple ground-based and space-based ionospheric observations, and the TIEGCM simulation. The ionosphere near the $F_2$ peak at low latitudes around the longitude of 110°E showed a strong negative storm effect during 12–18 UT on 2 October, whereas the GRACE and MetOp-A upward looking TECs in Southeast Asia did not suffer such depletions or even showed increases. The simultaneous ionospheric observations

indicated that the primary depletions of the negative ionospheric storm effect occurred around the $F_2$ peak height. The TIEGCM results and observations demonstrated that the contrasting behavior of the $F_2$ peak and the topside ionosphere could be primarily associated with the enhanced equatorward winds, which tend to transport the $F$ region ionosphere at low and middle latitudes into the equatorial topside ionosphere.

## References

Arendt, P. R. (1969), Comparison of the topside ionosphere during magnetic storms of various types, *Planet. Space Sci.*, *17*, 1993–1995, doi:10.1016/0032-0633(69)90136-6.

Astafyeva, E. I., I. Zakharenkova, and E. Doornbos (2015), Opposite hemispheric asymmetries during the ionospheric storm of 29-31 August 2004, *J. Geophys. Res. Space Physics*, *120*, 697–714, doi:10.1002/2014JA020710.

Bauer, S., and B. Krishnamurthy (1968), Behavior of the topside ionosphere during a great magnetic storm, *Planet. Space Sci.*, *16*, 653–663, doi:10.1016/0032-0633(68)90104-9.

Belehaki, A., and I. Tsagouri (2002), Investigation of the relative bottomside/topside contribution to the total electron content estimates, *Ann. Geophys.*, *45*, 73–86, doi:10.4401/AG-3498.

Blanc, M., and A. D. Richmond (1980), The ionospheric disturbance dynamo, *J. Geophys. Res.*, *85*, 1669–1686, doi:10.1029/JA085IA04P01669.

Blewitt, G. (1990), An automatic editing algorithm for GPS data, *Geophys. Res. Lett.*, *17*, 199–202, doi:10.1029/GL017I003P00199.

Buonsanto, M. J. (1999), Ionospheric storms—A review, *Space Sci. Rev.*, *88*, 563–601, doi:10.1023/A:1005107532631.

Burns, A. G., T. L. Killeen, W. Deng, G. R. Carignan, and R. G. Roble (1995), Geomagnetic storm effects in the low-latitude to middle-latitude upper thermosphere, *J. Geophys. Res.*, *100*, 14,673–14,691, doi:10.1029/94JA03232.

Chen, X., J. Lei, W. Wang, A. G. Burns, X. Luan, and X. Dou (2016), A numerical study of nighttime ionospheric variations in the American sector during 28–29 October 2003, *J. Geophys. Res. Space Physics*, *121*, doi:10.1002/2016JA023091.

Fatkullin, M. N. (1972), Topside ionosphere disturbance effects during different phases of two successive magnetic storms in September, 1963, *Planet. Space Sci.*, *20*, 627–636, doi:10.1016/0032-0633(72)90094-3.

Gonzalez, W. D., J. A. Joselyn, Y. Kamide, H. W. Kroehl, G. Rostoker, B. T. Tsurutani, and V. M. Vasyliunas (1994), What is a geomagnetic storm?, *J. Geophys. Res.*, *99*, 5771–5792, doi:10.1029/93JA02867.

Klobuchar, J. A. (1996), Ionospheric effects on GPS, in *Global Positioning System: Theory and Applications*, vol. 1, edited by B. W. Parkinson and J. J. Spilker, pp. 485–515, Am. Inst. of Aeronaut. and Astronaut., New York.

Lee, C.-K., S.-C. Han, D. Bilitza, and J.-K. Chung (2011), Validation of international reference ionosphere models using in situ measurements from GRACE K-band ranging system and CHAMP planar Langmuir probe, *J. Geod.*, *85*, 921–929, doi:10.1007/s00190-011-0442-6.

Lei, J., W. Wang, A. G. Burns, X. Yue, X. Dou, X. Luan, S. C. Solomon, and Y. C.-M. Liu (2014a), New aspects of the ionospheric response to the October 2003 superstorms from multiple-satellite observations, *J. Geophys. Res. Space Physics*, *119*, 2298–2317, doi:10.1002/2013JA019575.

Lei, J., W. Wang, J. P. Thayer, X. Luan, X. Dou, A. G. Burns, and S. C. Solomon (2014b), Simulations of the equatorial thermosphere anomaly: Geomagnetic activity modulation, *J. Geophys. Res. Space Physics*, *119*, 6821–6832, doi:10.1002/2014JA020152.

Lei, J., Q. Zhu, W. Wang, A. G. Burns, B. Zhao, X. Luan, J. Zhong, and X. Dou (2015), Response of the topside and bottomside ionosphere at low and middle latitudes to the October 2003 superstorms, *J. Geophys. Res. Space Physics*, *120*, 6974–6986, doi:10.1002/2015JA021310.

Mannucci, A. J., B. D. Wilson, D. N. Yuan, C. H. Ho, U. J. Lindqwister, and T. F. Runge (1998), A global mapping technique for GPS-derived ionospheric total electron content measurements, *Radio Sci.*, *33*, 565–582, doi:10.1029/97RS02707.

Mao, T., L. Sun, L. Hu, Y. Wang, and Z. Wang (2015), A case study of ionospheric storm effects in the Chinese sector during the October 2013 geomagnetic storm, *Adv. Space Res.*, *56*, 2030–2039, doi:10.1016/J.ASR.2015.05.045.

Mendillo, M. (2006), Storms in the ionosphere: Patterns and processes for total electron content, *Rev. Geophys.*, *44*, RG4001, doi:10.1029/2005RG000193.

Prölss, G. W. (1995), Ionospheric F-region storms, in *Handbook of Atmospheric Electrodynamics*, edited by H. Volland, pp. 195–248, CRC Press, Boca Raton, Fla.

Reinisch, B. W., and I. A. Galkin (2011), Global Ionospheric Radio Observatory (GIRO), *Earth Planets Space*, *63*, 377–381, doi:10.5047/EPS.2011.03.001.

Richmond, A. D., and G. Lu (2000), Upper-atmospheric effects of magnetic storms: A brief tutorial, *J. Atmos. Sol. Terr. Phys.*, *62*, 1115–1127, doi:10.1016/S1364-6826(00)00094-8.

Richmond, A. D., E. C. Ridley, and R. G. Roble (1992), A Thermosphere/Ionosphere General Circulation Model with coupled electrodynamics, *Geophys. Res. Lett.*, *19*, 601–604, doi:10.1029/92GL00401.

Rishbeth, H. (1998), How the thermospheric circulation affects the ionospheric F2-layer, *J. Atmos. Sol. Terr. Phys.*, *60*, 1385–1402, doi:10.1016/S1364-6826(98)00062-5.

Singh, N., and J. L. Horwitz (1992), Plasmasphere refilling: Recent observations and modeling, *J. Geophys. Res.*, *97*(A2), 1049–1079, doi:10.1029/91JA02602.

Tapley, B. D., S. Bettadpur, M. Watkins, and C. Reigber (2004), The gravity recovery and climate experiment: Mission overview and early results, *Geophys. Res. Lett.*, *31*, L09607, doi:10.1029/2004GL019920.

Weimer, D. R. (2005), Improved ionospheric electrodynamic models and application to calculating Joule heating rates, *J. Geophys. Res.*, *110*, A05306, doi:10.1029/2004JA010884.

Yu, T., C. Huang, G. Zhao, T. Mao, Y. Wang, Z. Zeng, J. Wang, and C. Xia (2014), A preliminary study of thermosphere and mesosphere wind observed by Fabry-Perot over Kelan, China, *J. Geophys. Res. Space Physics*, *119*, 4981–4997, doi:10.1002/2013JA019492.

Yue, X., W. S. Schreiner, D. C. Hunt, C. Rocken, and Y.-H. Kuo (2011), Quantitative evaluation of the low Earth orbit satellite based slant total electron content determination, *Space Weather*, *9*, S09001, doi:10.1029/2011SW000687.

Zhao, B., W. Wan, J. Lei, Y. Wei, Y. Sahai, and B. Reinisch (2012), Positive ionospheric storm effects at Latin America longitude during the superstorm of 20–22 November 2003: Revisit, *Ann. Geophys.*, *30*, 831–840, doi:10.5194/ANGEO-30-831-2012.

Zhong, J., J. Lei, X. Dou, and X. Yue (2016a), Is the long-term variation of the estimated GPS differential code biases associated with ionospheric variability?, *GPS Solutions*, *20*, 313–319, doi:10.1007/S10291-015-0437-5.

Zhong, J., J. Lei, X. Yue, and X. Dou (2016b), Determination of differential code bias of GNSS receiver onboard low Earth orbit satellite, *IEEE Trans. Geosci. Remote Sens.*, *54*, 4896–4905, doi:10.1109/TGRS.2016.2552542.

Zhong, J., J. Lei, X. Dou, and X. Yue (2016c), Assessment of vertical TEC mapping functions for space-based GNSS observations, *GPS Solutions*, *20*, 353–362, doi:10.1007/S10291-015-0444-6.

Zhong, J., W. Wang, X. Yue, A. G. Burns, X. Dou, and J. Lei (2016d), Long-duration depletion in the topside ionospheric total electron content during the recovery phase of the March 2015 strong storm, *J. Geophys. Res. Space Physics*, *121*, 4733–4747, doi:10.1002/2016JA022469.

Zhu, Q., J. Lei, X. Luan, and X. Dou (2016), Contribution of the topside and bottomside ionosphere to the total electron content during two strong geomagnetic storms, *J. Geophys. Res. Space Physics*, *121*, 2475–2488, doi:10.1002/2015JA022111.